

## Article

# Adsorption of Eriochrome Black T on Pseudo Boehmite and Gamma Alumina Synthesized from Drinking Water Treatment Sludge: A Waste-to-Recycling Approach

Ibtissam Ballou <sup>1,\*</sup> , Jamal Naja <sup>1</sup>, Zineelabidine Bakher <sup>2</sup> and Sanae Kholtei <sup>1</sup>

<sup>1</sup> Laboratory of Applied Chemistry and Environment, Faculty of Sciences and Techniques, Hassan First University of Settat, Settat 26000, Morocco; jamal.naja@uhp.ac.ma (J.N.); sanae.kholtei@uhp.ac.ma (S.K.)

<sup>2</sup> Laboratory of Physical Chemistry of Processes and Materials, Faculty of Sciences and Techniques, Hassan First University of Settat, Settat 26000, Morocco; zineelabidine.bakher@uhp.ac.ma

\* Correspondence: i.ballou@uhp.ac.ma

**Abstract:** Eriochrome black T is considered as one of the anionic dyes with potential harmful effects on human health and the environment. Among other processes, adsorption can contribute to the removal of these dyes. In the present study, two adsorbent materials, pseudo-boehmite ( $\gamma$ -AlOOH) and gamma alumina ( $\gamma$ -Al<sub>2</sub>O<sub>3</sub>), were synthesized and tested in the removal of the Eriochrome black T molecule (EBT).  $\gamma$ -AlOOH and  $\gamma$ -Al<sub>2</sub>O<sub>3</sub> were obtained by precipitation from NaAlO<sub>2</sub> solution at pH = 7, at a temperature of 80 °C, and by the thermal transformation of  $\gamma$ -AlOOH at 800 °C, respectively. In order to gain insights into the structural, chemical, thermal and morphological properties of these materials, numerous analytical techniques were involved, including X-ray diffraction (XRD), Fourier-transform infrared spectroscopy (FTIR), differential thermogravimetric–thermal analysis (TGA-DTA), scanning electron microscopy with energy-dispersive spectroscopy (SEM-EDS), and specific surface area measurement using the Brunauer–Emmett–Teller (BET) method. Several adsorption parameters were studied, such as the adsorbent dose, initial concentration, pH, contact time and reaction temperature. The kinetic study showed that EBT adsorption follows the pseudo-second-order model. The Langmuir isotherm model revealed a maximum EBT adsorption capacity of 344.44 mg g<sup>-1</sup> and 421.94 mg g<sup>-1</sup> for  $\gamma$ -AlOOH and  $\gamma$ -Al<sub>2</sub>O<sub>3</sub>, respectively. A textural and structural analysis after adsorption highlighted the effective adsorption of the dye.

**Keywords:** precipitation; pseudo-boehmite; gamma alumina; adsorption; eriochrome black T



**Citation:** Ballou, I.; Naja, J.; Bakher, Z.; Kholtei, S. Adsorption of Eriochrome Black T on Pseudo Boehmite and Gamma Alumina Synthesized from Drinking Water Treatment Sludge: A Waste-to-Recycling Approach. *Recycling* **2024**, *9*, 49. <https://doi.org/10.3390/recycling9030049>

Academic Editor: Julio Sacramento Rivero

Received: 21 April 2024

Revised: 16 May 2024

Accepted: 18 May 2024

Published: 4 June 2024



**Copyright:** © 2024 by the authors. Licensee MDPI, Basel, Switzerland. This article is an open access article distributed under the terms and conditions of the Creative Commons Attribution (CC BY) license (<https://creativecommons.org/licenses/by/4.0/>).

## 1. Introduction

In recent decades, the contamination of water resources by wastewater has become a crucial issue. A considerable volume of these wastewaters come from dyeing water, which is estimated at about 3 to 4 million cubic meters per day [1]. Indeed, dye waters contain a variety of chemical dyes that can be classified into different categories according to their application; azo dyes are the most frequently encountered dyes, and are known for their distinctive Azo groups (-N=N-). These dyes have been associated with various undesirable carcinogenic and mutagenic effects on human health and water quality [2]. In order to reduce the impact of these dyes on flora and fauna, it is therefore imperative to develop efficient technologies. Coagulation–flocculation [3], photocatalysis [4] and adsorption [5] are some of the widely used methods for dye removal. However, adsorption remains the most promising fading technique due to its straightforward implementation, high efficiency for adsorbent materials, and cost-effectiveness [6]. Pseudo-boehmite and gamma alumina are two potential adsorbents with numerous intriguing characteristics, including a high specific surface area, significant porosity, excellent thermal stability and remarkable chemical resistance; their versatility makes them suitable for many industrial applications, including ceramics, coatings and adhesives, and fillers. Additionally, they have proven

to be valuable in environmental applications, particularly as adsorbents and catalysts in wastewater treatment; they have been employed for the removal of dyes [7], fluoride [8], heavy metals [9] and phosphorus [10].

Boehmite with different morphologies has been developed using various methods, including precipitation [11], the sol-gel process [12], the hydrothermal route [13] and spray drying [1]. Most of these methods are costly and rely on the use of aluminum salts. Thus, aluminum recovered from aluminum sludge should be a more attractive candidate from an economic and environmental point of view. For this purpose, aluminum sludge has been thermo-chemically treated and solubilized with distilled water to extract aluminum [14].

The present study focused mainly on the synthesis of pseudo-boehmite by precipitation. After calcination, the obtained gamma alumina and pseudo-boehmite were characterized by several spectral and textural techniques. These materials were tested in terms of their adsorption capacity using the model molecule “Eriochrome Black T”. The decolorization performance has been optimized as a function of operating parameters such as the solution’s pH, initial adsorbent mass, initial dye concentration and contact time. The examination of Eriochrome black T removal using the two adsorbents showed that the adsorption isotherms follow the Langmuir model, while the adsorption kinetics follow the pseudo-second-order model.

## 2. Results and Discussions

### 2.1. Adsorbents Characterization

#### 2.1.1. XRD Analysis

The XRD pattern of the dried precipitate showed that a pseudo-boehmite phase ( $\gamma$ -AlOOH) was formed (ICSD 00-21-1307), as shown in Figure 1a. No phases related to iron, calcium, or magnesium hydroxides were observed, suggesting that these impurities were likely eliminated during the precipitation at an alkaline pH. The characteristic peaks of the  $\gamma$ -AlOOH phase are apparent at  $2\theta$  ( $14.4^\circ$ ,  $28.2^\circ$ ,  $38.3^\circ$ ,  $49.2^\circ$ ,  $55.2^\circ$ ,  $60.5^\circ$ ,  $64.9^\circ$ , and  $71.9^\circ$ ), and these correspond to reflections from the (020), (120), (031), (200)/(051), (151), (080), (231)/(002), and (251) planes, respectively. At the same pH value of 7, the same phase has been detected in previous work [15,16]. During the precipitation stage, the structure of aluminum hydroxide can vary depending on the pH. At  $\text{pH} < 7$ , it exists in an amorphous form, at  $\text{pH} = 7$ , it takes on the form of boehmite, and within the pH range of 8 to 11, it is in the form of Bayerite [17].

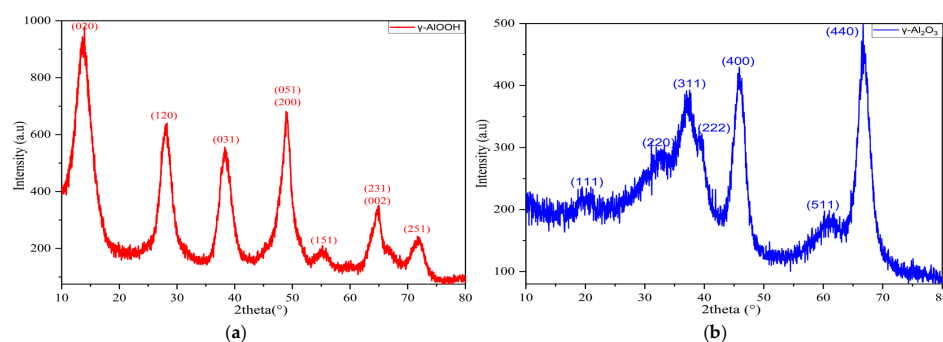


**Figure 1.** XRD patterns of  $\gamma$ -AlOOH (a) and  $\gamma$ -Al<sub>2</sub>O<sub>3</sub> particles (b).

An examination of the XRD patterns displayed in Figure 1b shows that after calcination, the  $\gamma$ -AlOOH peaks disappear completely and  $\gamma$ -Al<sub>2</sub>O<sub>3</sub> peaks appear, becoming increasingly intense at 800 °C. The peaks identified at  $37.6^\circ$ ,  $39.49^\circ$ ,  $45.86^\circ$ ,  $60.94^\circ$ , and  $67.06^\circ$  correspond to reflections from the (311), (222), (400), (511) and (440) planes of the  $\gamma$ -Al<sub>2</sub>O<sub>3</sub> structure (ICSD 00-10-0425).

The particle size of  $\gamma$ -AlOOH and  $\gamma$ -Al<sub>2</sub>O<sub>3</sub> was calculated from the XRD data using the Debye-Scherrer formula [18]:

$$D = \frac{k\lambda}{\beta \cos\theta}$$

where  $k$  is the Scherrer constant, also known as the form factor; typically, its value ranges from 0.89 to 1. Assuming the particles have a spherical shape, the Scherrer constant is commonly assigned a value of 0.9. Other variables in the equation include  $\lambda$ , which represents the X-ray wavelength,  $\theta$ , which denotes the diffraction angle, and  $\beta$ , which represents the total width at half maximum (FWHM); the latter measures the crystallinity of a sample. The average crystallite sizes of  $\gamma$ -AlOOH and  $\gamma$ -Al<sub>2</sub>O<sub>3</sub>, calculated using reflections (020), (120), (031), (200), (231), (251) and (220), (311), (222), (400), (440), are 3.63 and 3.06 nm, respectively. These results are consistent with the typical values reported in the literature [19,20].

### 2.1.2. FTIR Analysis

The FTIR spectrum of  $\gamma$ -AlOOH is illustrated in Figure 2a; the broad band located at 3440 cm<sup>-1</sup> and the band at 1639 cm<sup>-1</sup> are attributed to the stretching and bending modes of physically adsorbed water, respectively [19]. Although the band at 3440 cm<sup>-1</sup> dominates the region, the band at 3315 cm<sup>-1</sup>, characteristic of the stretching vibrations of the structural OH group, can be identified [1]. The shoulder at 3093 cm<sup>-1</sup> is associated with the (Al)O-H stretching vibration of  $\gamma$ -AlOOH [19]. The weak band at 2090 cm<sup>-1</sup> is assigned to the AlO<sub>4</sub> combination band [21]. The two vibrations at 1520 and 1400 cm<sup>-1</sup> are due to the presence of the amorphous structure on the surface of  $\gamma$ -AlOOH [19]. The band at 1072 cm<sup>-1</sup> is attributed to the asymmetric stretching vibration (OH)-Al=O, while the shoulder around 1170 cm<sup>-1</sup> corresponds to the bending vibration (O-H) [22]. The bands at 760, 625 and 488 cm<sup>-1</sup> are associated with the AlO<sub>6</sub> vibrational modes typical of  $\gamma$ -AlOOH [23].

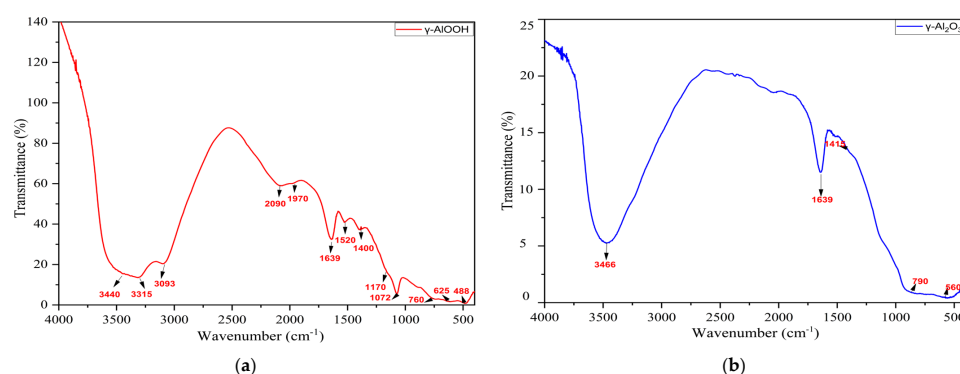


**Figure 2.** FTIR spectra of  $\gamma$ -AlOOH (a),  $\gamma$ -Al<sub>2</sub>O<sub>3</sub> (b).

The presence of the  $\gamma$ -Al<sub>2</sub>O<sub>3</sub> phase is confirmed by the broad band observed between 500 cm<sup>-1</sup> and 800 cm<sup>-1</sup> [11], as depicted in Figure 2b. The two peaks at 560 cm<sup>-1</sup> and 790 cm<sup>-1</sup> are assigned to Al-O stretching [24]. The identification of the band at 1136 cm<sup>-1</sup>, which corresponds to the Al-O vibration mode, supports the formation of the  $\gamma$ -Al<sub>2</sub>O<sub>3</sub> phase [25]. The shoulder at 1415 cm<sup>-1</sup> is attributed to O-H bending [24]. Similar to the spectra of  $\gamma$ -AlOOH, the  $\gamma$ -Al<sub>2</sub>O<sub>3</sub> spectra exhibit two characteristic bands at 3466 cm<sup>-1</sup> and 1639 cm<sup>-1</sup>, which are indicative of the presence of physically adsorbed water.

### 2.1.3. TGA and TDA Analysis

The TGA and DTA curves for  $\gamma$ -AlOOH particles are shown in Figure 3. The first weight loss of 14.6% observed below 170 °C, associated with a first endothermic peak at 130 °C in the DTA curve, is ascribed to the evaporation of physically adsorbed water; gelling boehmite or pseudo-boehmite showed an excess water weight loss of 15% [26]. A second weight loss of 14.7% occurs over a wider temperature range of 170 to 570 °C, which is associated with a second endothermic peak at 400 °C; this could be attributed to a phase transition from  $\gamma$ -AlOOH to the  $\gamma$ -Al<sub>2</sub>O<sub>3</sub> ( $2\gamma$ -AlOOH →  $\gamma$ -Al<sub>2</sub>O<sub>3</sub> + H<sub>2</sub>O). The same transition phase has been recorded by other authors at a temperature of 464 °C for a crystallite size of the order of 5 nm [22], indicating that the larger the crystallite size, the

higher the transition temperature. Between 570 and 800 °C, a non-significant decrease of 0.3% was observed, which could be attributed to the elimination of the residual hydroxyl groups (-OH) present in the Al<sub>2</sub>O<sub>3</sub> structure.

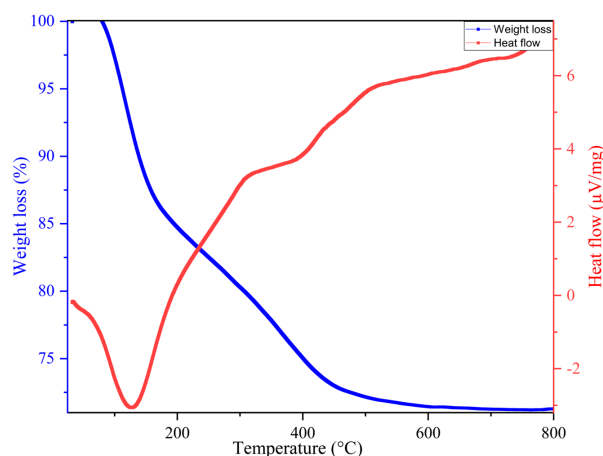


**Figure 3.** TGA/DTA curves of  $\gamma$ -AlOOH.

#### 2.1.4. BET Analysis

To further investigate the structure of  $\gamma$ -AlOOH and  $\gamma$ -Al<sub>2</sub>O<sub>3</sub>, we recorded the typical adsorption–desorption isotherms for N<sub>2</sub> (Figure 4). The sorption isotherms exhibit the type IV characteristic of mesoporous materials, according to the (IUPAC) classification. An H<sub>2</sub>-type hysteresis loop is observed in the  $p/p_0$  relative pressure range of 0.45 to 0.92, which could correspond to mesopores. Furthermore, no plateau was observed for relatively high pressures in the range of 0.92 to 1.00, suggesting an H<sub>3</sub>-type hysteresis loop; this indicates the possibility of particle agglomerate development.

Figure 4 shows that the adsorbed volume of gas has increased from 160 cm<sup>3</sup> g<sup>-1</sup> (Figure 4a) to 220 cm<sup>3</sup> g<sup>-1</sup> (Figure 4b); an improvement in the specific surface area of  $\gamma$ -AlOOH is produced during its thermal conversion to  $\gamma$ -Al<sub>2</sub>O<sub>3</sub>, increasing from 298.35 to 403.31 m<sup>2</sup> g<sup>-1</sup>. These values are higher than those reported for the synthesis of these two materials using aluminum waste as a precursor [7,15]. In fact,  $\gamma$ -Al<sub>2</sub>O<sub>3</sub> with a specific surface area of 304.21 m<sup>2</sup> g<sup>-1</sup> was obtained from aluminum frame waste [7], while  $\gamma$ -AlOOH and  $\gamma$ -Al<sub>2</sub>O<sub>3</sub> with specific surface areas of 115 and 300 m<sup>2</sup> g<sup>-1</sup>, respectively, were obtained from paper pulp waste [15]. This variation in the specific surface area could be attributed to several factors, including differences in the precursor material, synthesis conditions such as the pH, temperature, and ageing time, as well as the calcination temperature. Indeed, the  $\gamma$ -Al<sub>2</sub>O<sub>3</sub> obtained from calcination at 1000 °C has a high surface area compared to the  $\gamma$ -Al<sub>2</sub>O<sub>3</sub> produced through calcination at 900 °C [9].

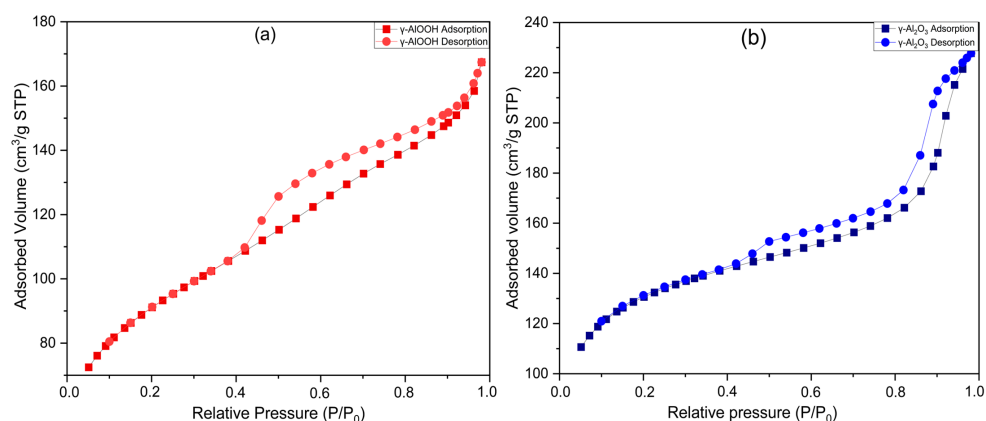


**Figure 4.** Nitrogen adsorption–desorption isotherms of  $\gamma$ -AlOOH (a) and  $\gamma$ -Al<sub>2</sub>O<sub>3</sub> (b).

### 2.1.5. SEM Analysis

In order to examine the morphology of  $\gamma$ -AlOOH and  $\gamma$ -Al<sub>2</sub>O<sub>3</sub>, the samples were characterized by SEM (Figure 5). The particles appear as non-rigid aggregates forming clusters with a flake-like structure, with some tiny particles also detected. Similar morphological characteristics have been observed in the literature [7,10]. In addition to SEM analysis, EDS analysis was carried out. The chemical composition of the  $\gamma$ -AlOOH (Al wt.%:  $51.6 \pm 0.8$ ; O wt.%:  $48.3 \pm 0.7$ ) and  $\gamma$ -Al<sub>2</sub>O<sub>3</sub> (Al wt.%:  $54.6 \pm 0.9$ ; O wt.%:  $45.3 \pm 0.7$ ) synthesized from the sludge shows that both products exhibited high purity.

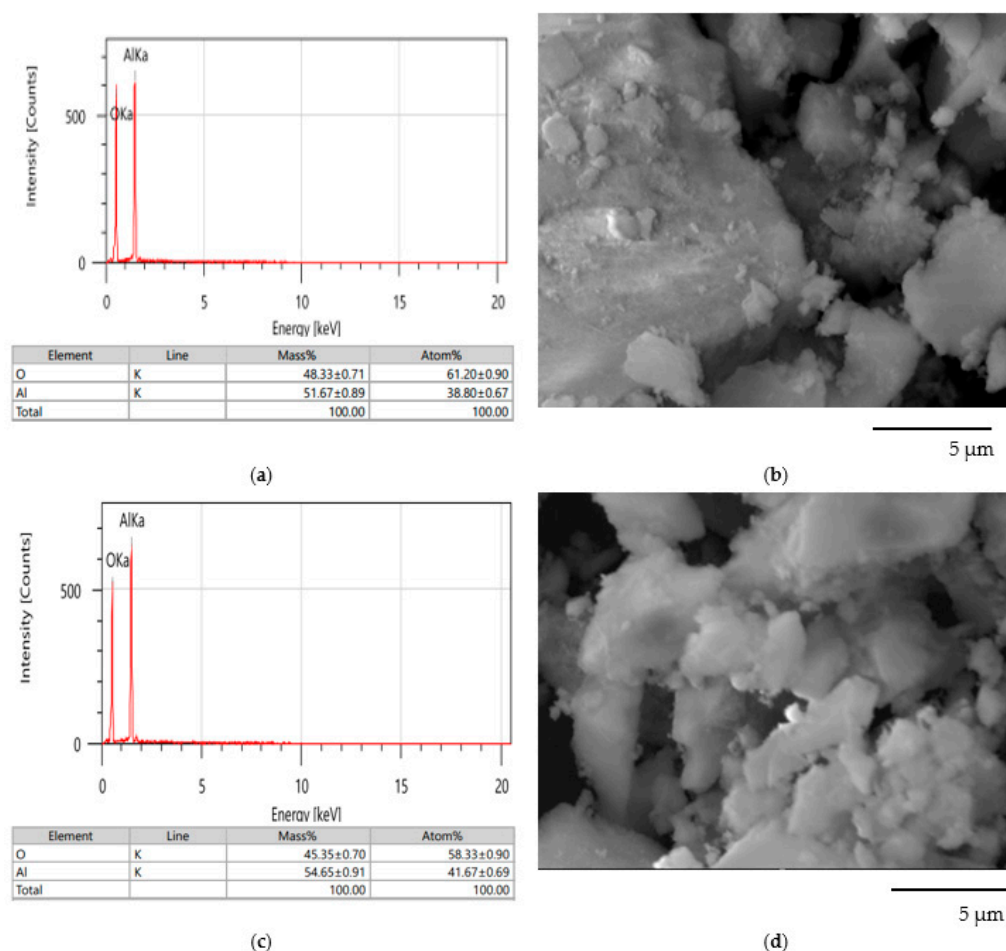


**Figure 5.** EDS spectrum; EDS elemental composition (a), SEM image (b) of  $\gamma$ -AlOOH/EDS spectrum; EDS elemental composition (c), SEM image (d) of  $\gamma$ -Al<sub>2</sub>O<sub>3</sub>.

### 2.1.6. The Adsorbents' Point of Zero Charge

The point of zero charge ( $\text{pH}_{\text{pzc}}$ ) is an important physico-chemical parameter providing information on the phenomena occurring at the surface of adsorbents. At a pH below  $\text{pH}_{\text{pzc}}$ , protonated adsorbent surface functional groups attract negatively charged adsorbates due to an excess  $\text{H}^+$ . At a pH above  $\text{pH}_{\text{pzc}}$ , the positively charged adsorbates are adsorbed onto the negatively charged adsorbent surface. Synthesized  $\gamma$ -AlOOH has a  $\text{pH}_{\text{pzc}}$  of 7, while  $\gamma$ -Al<sub>2</sub>O<sub>3</sub> has a  $\text{pH}_{\text{pzc}}$  of 7.3 (Figure 6). These values are in good agreement with the results cited by [1,7,11].

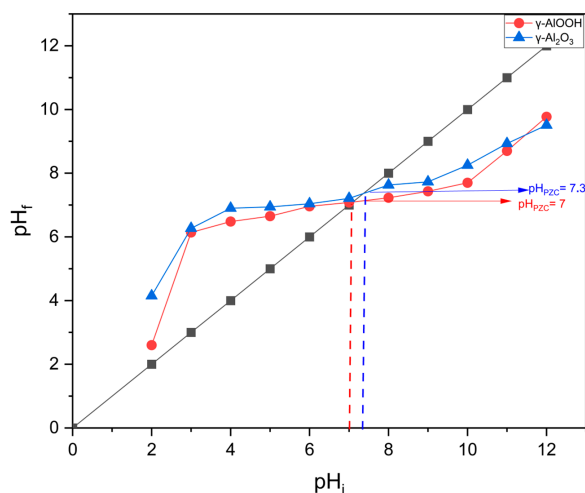


**Figure 6.** The pH of point zero charge ( $pH_{PZC}$ ) of  $\gamma$ -AlOOH and  $\gamma$ -Al<sub>2</sub>O<sub>3</sub>.

## 2.2. Batch Studies on the Adsorption of EBT onto $\gamma$ -AlOOH and $\gamma$ -Al<sub>2</sub>O<sub>3</sub>

### 2.2.1. Effect of Initial pH

As pH is an important factor affecting both adsorbent and adsorbate surface charge, the effect of pH on EBT removal was examined over a pH range of 3 to 12. As shown in Figure 7, the removal efficiency is highest at an acidic pH, decreases slightly at a pH above 7 and then decreases sharply at a pH above 10 for both tested adsorbents. Significant elimination occurs under acidic conditions, taking into account the protonation state of the dye (EBT occurs as a monovalent anion at  $pH > 3.9$ ) and the positively charged surface of both adsorbents. At  $pH < pH_{PZC}$ , EBT adsorption is favored by the electrostatic attraction forces between the sulfonic groups ( $SO_3^-$ ) and the acidic surface ( $Al-OH_2^+$ ) of both adsorbents. As the pH approaches the pH of point zero charge, adsorption occurs through the formation of hydrogen bonds between the hydroxyl groups on the surface ( $Al-OH$ ) and the OH and  $NO_2$  groups of the EBT.

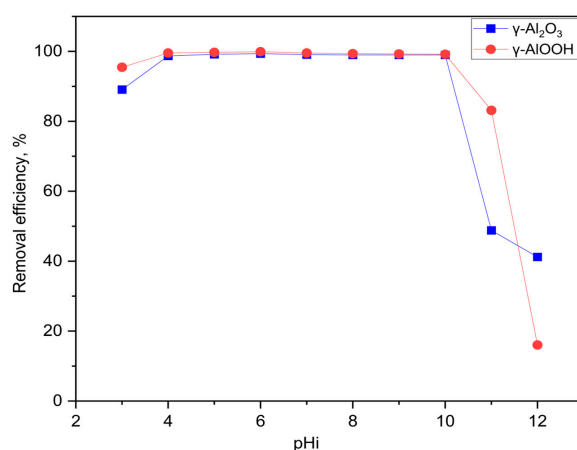


**Figure 7.** Effect of pH on the efficiency of removing EBT by  $\gamma$ -AlOOH and  $\gamma$ -Al<sub>2</sub>O<sub>3</sub>; Mass = 50 mg,  $C_0$  [EBT] = 50 mg L<sup>-1</sup>, V = 50 mL.

It is important to note that at a pH slightly above  $pH_{PZC}$ , the surfaces of  $\gamma$ -AlOOH and  $\gamma$ -Al<sub>2</sub>O<sub>3</sub> become negatively charged due to surface deprotonation ( $Al-O^-$ ), producing electrostatic repulsion between the adsorbent and adsorbate. However, the removal efficiency is also significant, which may be due to the  $Al^{3+}$  sites on the surface trapping the EBT sulfonate group. At  $pH > 10$ , the removal efficiency is reduced due to the onset of adsorbent solubilization. Maximum EBT removal is achieved at  $pH = 5$ , and subsequent experiments are carried out at the initial solution pH (5.78).

### 2.2.2. Effect of Adsorbent Mass

To study the effect of the adsorbent mass on EBT adsorption, experiments were conducted at an initial concentration of  $50 \text{ mg L}^{-1}$  and at the initial pH of the dye solution. It can be seen from Figure 8 that the removal efficiency increases progressively as the adsorbent mass increases from 5 mg up to 50 mg, rising from 63.24 to 99.44% and from 78.15 to 99.25% for  $\gamma\text{-AlOOH}$  and  $\gamma\text{-Al}_2\text{O}_3$ , respectively. This could be attributed to the number of accessible active sites. Above 50 mg, equilibrium is reached. Subsequent tests were carried out using this optimal adsorbent mass.

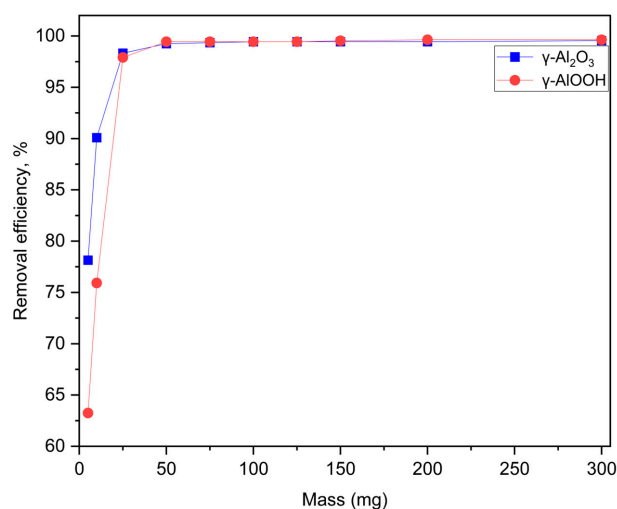


**Figure 8.** Effect of adsorbent initial mass ( $\gamma\text{-AlOOH}$  and  $\gamma\text{-Al}_2\text{O}_3$ ) on the efficiency of removing EBT; Mass (5–300 mg),  $C_0$  [EBT] =  $50 \text{ mg L}^{-1}$ ,  $V = 50 \text{ mL}$ .

### 2.2.3. Kinetic Studies

Figure 9 illustrates the effect of contact time on EBT adsorption by  $\gamma\text{-AlOOH}$  and  $\gamma\text{-Al}_2\text{O}_3$ . EBT adsorption follows rapid kinetics, reaching a near-equilibrium state after 20 min for both adsorbents. This could be justified by the availability of active sites for molecule binding and/or the high adsorbate/adsorbent affinity.

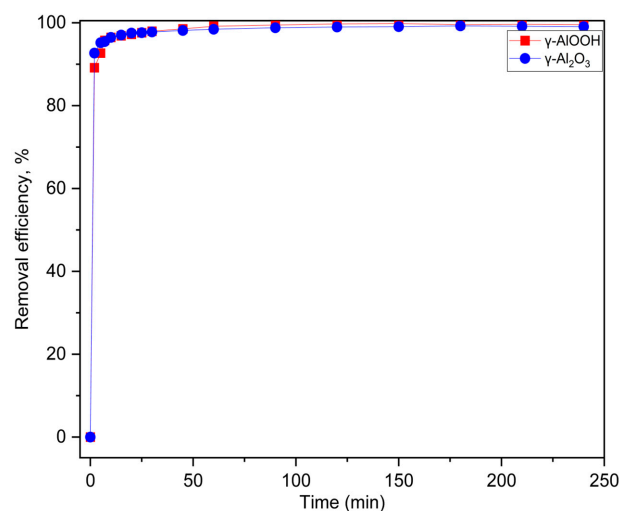


**Figure 9.** Effect of contact time on the adsorption of EBT onto  $\gamma\text{-AlOOH}$  and  $\gamma\text{-Al}_2\text{O}_3$ .

Three models, including the pseudo-first-order, the pseudo-second-order and intra-particle diffusion models (Figure 10), were used to adjust the experimental data. Tables 1 and 2 show the kinetic parameters associated with each model. The pseudo-second-order model has a correlation coefficient  $R^2$  (0.99) higher than the value obtained for the other

models. This indicates that the pseudo-second-order model best describes the adsorption data. The  $q_{e,cal}$  value predicted using the pseudo-second-order model was extremely similar to that of the adsorption equilibrium found experimentally. This finding demonstrates that the predominant underlying mechanism of EBT adsorption on  $\gamma$ -AlOOH and  $\gamma$ -Al<sub>2</sub>O<sub>3</sub> could be chemisorption, which therefore suggests that the ionic interaction or ion exchange between active sites and dye molecules controls the adsorption process [27] and that the adsorption rate is linearly related to the square of the amount of vacant sites [24]. These results agree with those of other authors using  $\gamma$ -AlOOH [1] and  $\gamma$ -Al<sub>2</sub>O<sub>3</sub> [28,29].

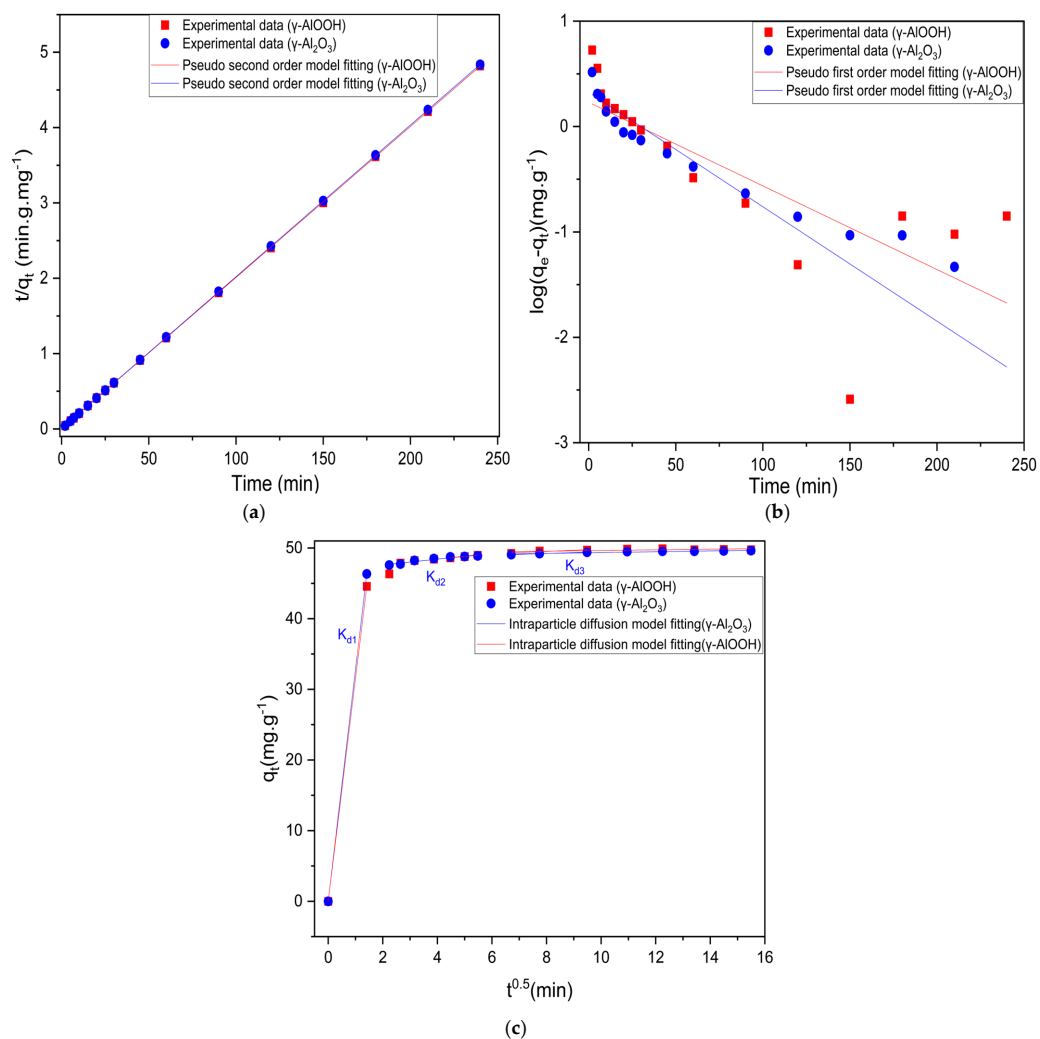


**Figure 10.** Plots of the pseudo-second order (a), pseudo-first-order (b) and intraparticle diffusion (c) kinetic models for EBT adsorption onto  $\gamma$ -AlOOH and  $\gamma$ -Al<sub>2</sub>O<sub>3</sub>.

**Table 1.** Pseudo-first-order and pseudo-second-order kinetics models' parameters for EBT adsorption.

	Pseudo-First-Order Model			Pseudo-Second-Order Model		
	$k_1$ (min <sup>-1</sup> )	R <sup>2</sup>	$q_{e,cal}$	$k_2$ (g mg <sup>-1</sup> min <sup>-1</sup> )	R <sup>2</sup>	$q_{e,cal}$
$\gamma$ -AlOOH	0.02	0.54	1.70	0.050	0.99	49.9
$\gamma$ -Al <sub>2</sub> O <sub>3</sub>	0.02	0.82	2.11	0.054	1	49.7



**Table 2.** Intraparticle diffusion model’s parameters for EBT adsorption.

	Step 1			Step 2			Step 3		
	$K_{d1}$	$R_1^2$	$C_1$	$K_{d2}$	$R_2^2$	$C_2$	$K_{d3}$	$R_3^2$	$C_3$
$\gamma$ -AlOOH	31.52	1	$2.51 \times 10^{-15}$	0.36	0.99	46.96	0.05	0.45	49.17
$\gamma$ -Al <sub>2</sub> O <sub>3</sub>	22.77	1	0	0.41	0.91	46.76	0.06	0.88	48.77

The intraparticle diffusion model for EBT is shown in Figure 10. The adsorption process appears to take place in three stages, as shown in this figure: the first stage, external adsorption, occurs at a faster rate than the second stage, which is known as slow adsorption; in this, there is a significant reduction in the adsorption rate due to the decrease in the dye concentration. The last stage, the equilibrium stage, is characterized by the lowest internal diffusion rate and the lowest dye concentration. The fitting parameters for this model are listed in Table 2. The results show that the adsorption rate decreases progressively ( $K_{d1} > K_{d2} > K_{d3}$ ) and that the effect of the boundary layer increases progressively ( $C_1 < C_2 < C_3$ ), which is consistent with the evolution of the adsorption rate during the adsorption phase. It can also be seen that the fitted line does not pass through the origin, which further suggests that intraparticle diffusion does not play a major role in controlling the adsorption rate and that several processes act simultaneously during adsorption [30].

2.2.4. Equilibrium Studies

As depicted in Figure 11a, the adsorption isotherms of  $\gamma$ -AlOOH and  $\gamma$ -Al<sub>2</sub>O<sub>3</sub> for EBT are type L. The adsorption capacity of  $\gamma$ -Al<sub>2</sub>O<sub>3</sub> is significantly higher than that of  $\gamma$ -AlOOH. Given that both adsorbents have a comparable surface chemistry and adsorb the same dye molecule (EBT), this difference could be explained by the greater specific surface area of  $\gamma$ -Al<sub>2</sub>O<sub>3</sub>. The adjustment of the experimental data to the Langmuir and Freundlich models is shown in Figure 11b,c. The Langmuir isotherm in its linear form is considered most appropriate because it provides a better fit with the highest ( $R^2 = 0.99$ ) compared to the Freundlich model, which had a correlation coefficient of about 0.96 (Table 3). This result could be identified with the monolayer adsorption of the dye. The maximum adsorption capacity ( $q_m$ ) calculated for the Langmuir model is of the order of  $344.44 \text{ mg g}^{-1}$  and  $421.94 \text{ mg g}^{-1}$  for  $\gamma$ -AlOOH and  $\gamma$ -Al<sub>2</sub>O<sub>3</sub>, respectively. Similar monolayer molecule-binding behavior was obtained for the removal of Congo red molecules using  $\gamma$ -AlOOH [1] and Methyl orange molecules using  $\gamma$ -Al<sub>2</sub>O<sub>3</sub> [28].

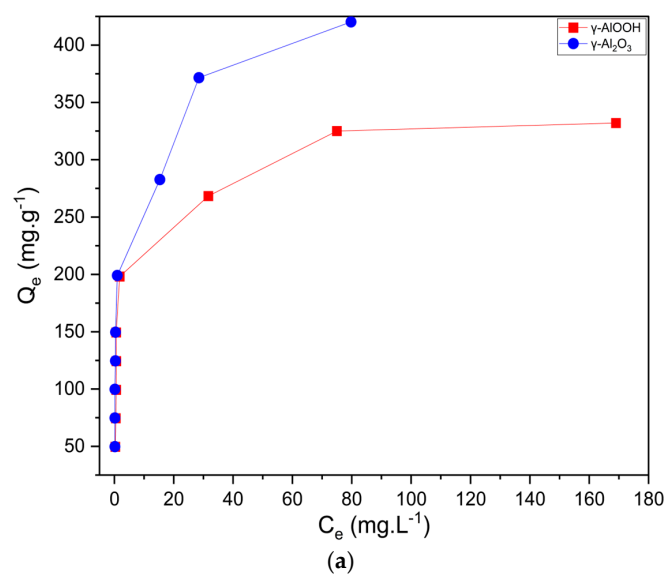


**Figure 11.** Cont.

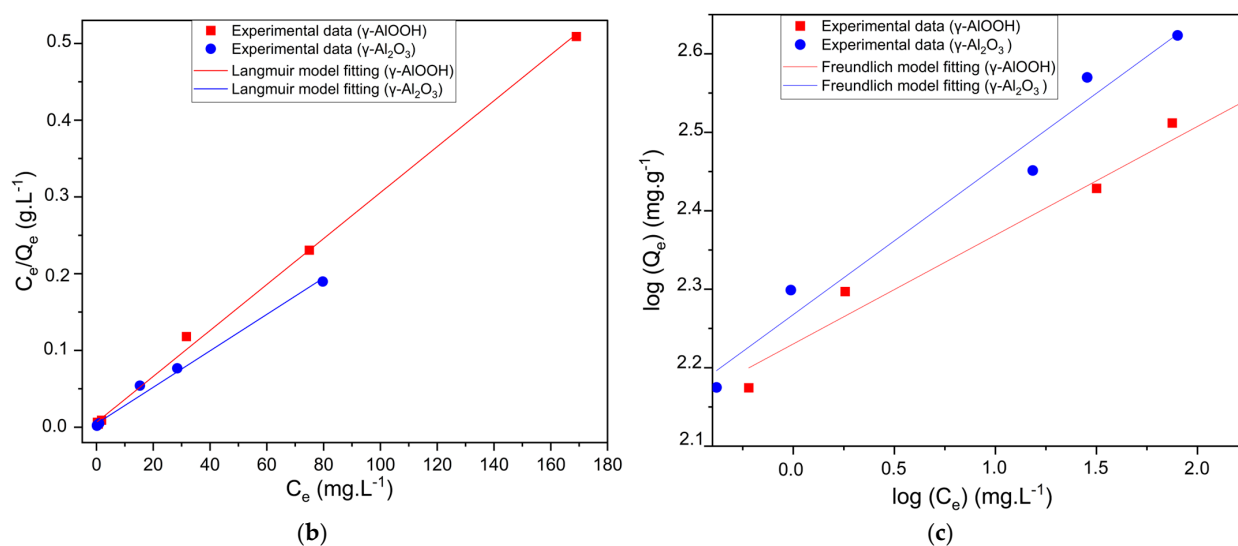


Figure 11. Adsorption isotherms of EBT adsorption onto  $\gamma$ -AlOOH and  $\gamma$ -Al<sub>2</sub>O<sub>3</sub> (a); modeling of the adsorption equilibrium by Langmuir (b) and Freundlich (c) isotherms.

Table 3. Langmuir and Freundlich isotherm models' parameters.

Adsorbent	Langmuir Model			Freundlich Model		
	q <sub>m</sub> (mg g <sup>-1</sup> )	K <sub>L</sub> (L mg <sup>-1</sup> )	R <sup>2</sup>	K <sub>F</sub> (mg <sup>1-(1/n)</sup> L <sup>1/n</sup> g <sup>-1</sup> )	n	R <sup>2</sup>
$\gamma$ -AlOOH	344.45	0.47	0.99	169.94	7.21	0.96
$\gamma$ -Al <sub>2</sub> O <sub>3</sub>	421.94	0.53	0.99	185.24	5.32	0.96

The equilibrium parameter defined by the formula  $R_L = \frac{1}{1+K_L C_i}$  can be used to study the feasibility of the Langmuir isotherm, where  $C_i$  (mg g<sup>-1</sup>) represents the initial EBT solution concentration. The value of  $R_L$  determines whether adsorption is favorable ( $0 < R_L < 1$ ) or unfavorable ( $R_L > 1$ ). The  $R_L$  values in the present study are greater than zero ( $R_{L\gamma\text{-AlOOH}} = 0.041$ ,  $R_{L\gamma\text{-Al}_2\text{O}_3} = 0.036$ ), confirming the favorable nature of EBT adsorption for both adsorbents.

### 2.2.5. Thermodynamic Study

The determination of the thermodynamic parameters for EBT adsorption was accomplished through Equations (8)–(10).

It was observed that the adsorption process utilizing both adsorbents is thermodynamically feasible and spontaneous, as demonstrated by the negative  $\Delta G^\circ$  values obtained. As the temperature increases,  $\Delta G^\circ$  decreases, indicating a greater preference for EBT adsorption at higher temperatures (Figure 12). The process is classified as endothermic, absorbing heat, as indicated by the positive  $\Delta H^\circ$ . The value of  $\Delta H^\circ$  is relatively low ( $\Delta H^\circ < 40$  KJ mol<sup>-1</sup>), suggesting that the adsorption is predominantly physisorption [31]. Moreover, the positive value of  $\Delta S^\circ$  reflects the presence of randomness at the solid–liquid interface and the stability of the adsorption process (Table 4).

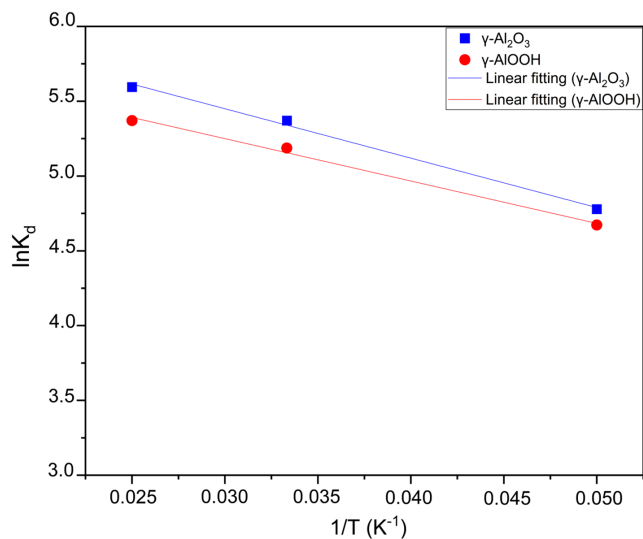


Figure 12. Plot of  $\ln K_d$  vs.  $1/T$  for the adsorption of EBT onto  $\gamma$ -AlOOH and  $\gamma$ -Al<sub>2</sub>O<sub>3</sub>.

Table 4. Thermodynamic parameters for EBT adsorption onto  $\gamma$ -AlOOH and  $\gamma$ -Al<sub>2</sub>O<sub>3</sub> at various temperatures.

Adsorbent	T(K)	$\Delta G^\circ$ (KJ mol <sup>-1</sup> )	$\Delta H^\circ$ (J mol <sup>-1</sup> )	$\Delta S^\circ$ (J mol <sup>-1</sup> K <sup>-1</sup> )
$\gamma$ -AlOOH	293	-14.622	235.75	50.71
	303	-15.129		
	313	-15.636		
$\gamma$ -Al <sub>2</sub> O <sub>3</sub>	293	-15.452	274.64	53.55
	303	-16.048		
	313	-16.524		

### 2.2.6. Investigation of the EBT Adsorption Process

Figure 13a,b illustrates the XRD patterns of  $\gamma$ -AlOOH and  $\gamma$ -Al<sub>2</sub>O<sub>3</sub> before and after adsorption; it can be seen that the peaks remain almost in the same  $2\theta$  positions, with a slight decrease in the peak intensity. This could indicate that only physical adsorption is involved and that there is no possible ion exchange phenomenon.

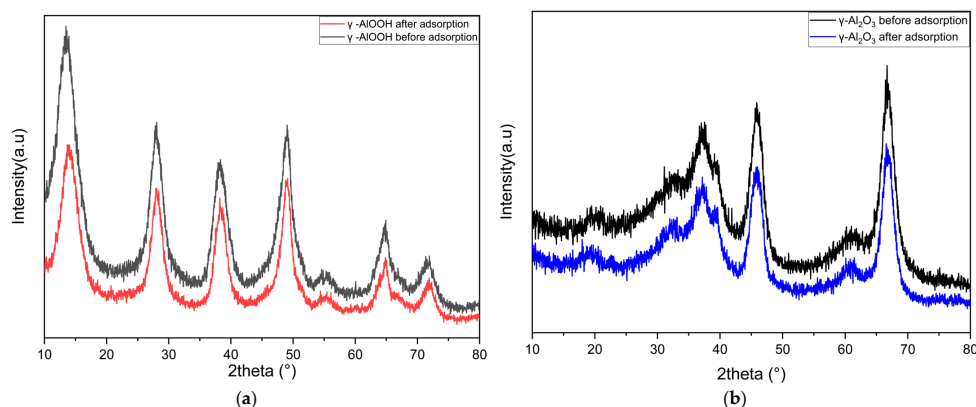
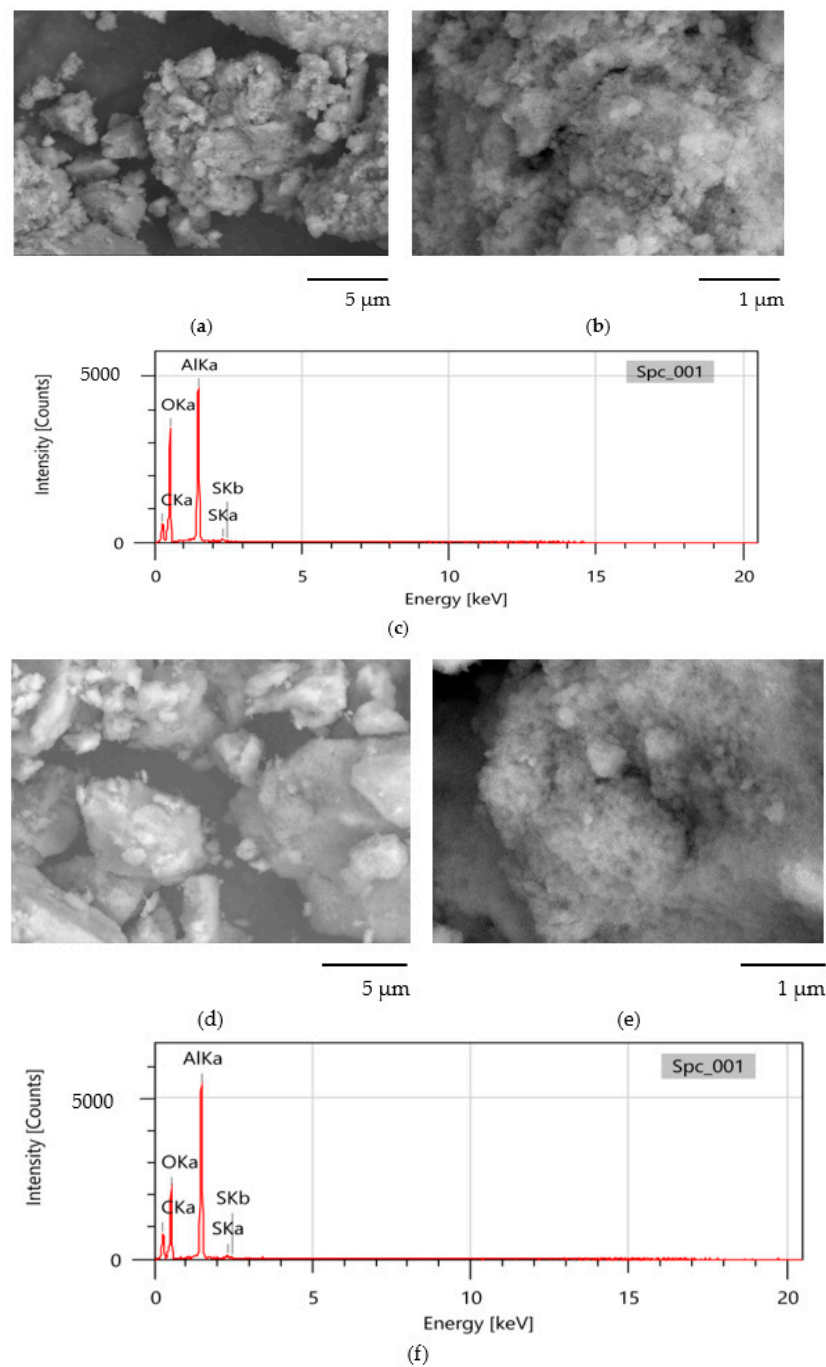


Figure 13.  $\gamma$ -AlOOH (a) and  $\gamma$ -Al<sub>2</sub>O<sub>3</sub> (b) XRD patterns before and after EBT adsorption.

Figure 14 shows the SEM images of  $\gamma$ -AlOOH (Figure 14a,b) and  $\gamma$ -Al<sub>2</sub>O<sub>3</sub> (Figure 14d,e) after dye adsorption. The surface morphology of both loaded materials showed no significant changes. However, surface roughness was noted. The EDS spectrum showed the appearance of the carbon (C) and sulfur (S) peaks of the adsorbed dye.



**Figure 14.** SEM images (a,b) and EDS spectrum (c) of  $\gamma$ -AlOOH after adsorption, and SEM images (d,e) and EDS spectrum (f) of  $\gamma$ -Al<sub>2</sub>O<sub>3</sub> after adsorption.

### 2.2.7. Comparison with Other Adsorbents

Table 5 presents the adsorption performance of  $\gamma$ -AlOOH and  $\gamma$ -Al<sub>2</sub>O<sub>3</sub> for EBT removal, along with the adsorption capacities reported in the literature for various adsorbents. The results indicate that the two adsorbents investigated in this study exhibit promising adsorption capacities for EBT compared to other adsorbents. Moreover, these adsorbents offer the additional advantage of being recycled from waste, making them economically advantageous for wastewater treatment applications.

**Table 5.** EBT's maximum adsorption capacity ( $q_m$ ) by various adsorbents.

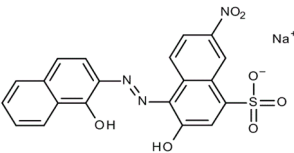
Adsorbents	$q_m$ (mg g <sup>-1</sup> )	References
Microwave-assisted spent black tea leaves	242.72	[32]
Arab steel slag	39.69	[33]
Biochar-CuFe	565.31	[34]
Mg-Ca-Al-LDO	150.3	[35]
$\gamma$ -AlOOH	344.21	This work
$\gamma$ -Al <sub>2</sub> O <sub>3</sub>	421.94	This work

### 3. Materials and Methods

#### 3.1. Materials

Eriochrome black T (EBT) is classified as an anionic dye belonging to the group of sulfonic azo dyes. It is used for the detection of metal ions in solution by the complexation method, and for dyeing woolen fabrics, silk, nylon and leather. Table 6 displays the chemical characteristics of the studied dye. The maximum spectral response of EBT was observed at a wavelength of 530 nm within the visible spectrum.

**Table 6.** Chemical properties of Eriochrome black T (EBT).

Dye	Chemical Formula	Structure	Molecular Weight (g mol <sup>-1</sup> )	Color Index
EBT	C <sub>20</sub> H <sub>12</sub> N <sub>3</sub> O <sub>7</sub> SNa		461.381	Mordant Black 11 [36]

All aqueous solutions were prepared in distilled water, and pH adjustments were made using sodium hydroxide NaOH (0.1 M) (98%) and hydrochloric acid HCl (0.1 M) (37%); 98% and 37% are the percentages of the pure reagents.

#### 3.2. Pseudo-Boehmite ( $\gamma$ -AlOOH) and Gamma Alumina ( $\gamma$ -Al<sub>2</sub>O<sub>3</sub>) Oxide Preparation

Aluminum extracted from drinking water treatment sludge by thermochemical treatment with ammonium sulfate was the subject of our study for the synthesis of  $\gamma$ -AlOOH and  $\gamma$ -Al<sub>2</sub>O<sub>3</sub> [14].

The resulting solution was heated to 80 °C. The pH was adjusted to 13 by adding NaOH solution (5 M) drop by drop for 40 min, which transformed Al(OH)<sub>3</sub> into Al(OH)<sub>4</sub><sup>-</sup> and prevented major impurities such as iron, calcium and magnesium hydroxides from passing into solution. The resulting alkaline sodium aluminate solution was heated up to 80 °C. To produce  $\gamma$ -AlOOH, HCl (5 M) was added dropwise to the filtrate until pH = 7 was reached under continuous stirring. The white gel formed was stirred for about 5 h, then left to age for 12 h with stirring. It was then filtered, washed with distilled water and ethanol several times, and dried at 110 °C overnight. Subsequently, it was calcined in a muffle furnace at 800 °C for 3 h, with a controlled heating rate of 2 °C/min. This rate was chosen to prevent rapid dehydration, ensure consistent pore structure, and avoid excessive grain growth [37].

#### 3.3. Characterization Techniques

The crystal structures of  $\gamma$ -AlOOH and  $\gamma$ -Al<sub>2</sub>O<sub>3</sub> were analyzed using a Bruker (Billerica, MA, USA) diffractometer (D2 Phaser) with monochromatized CuK <sub>$\alpha$</sub>  radiation ( $\lambda = 1.541$ ). Patterns were recorded in the  $2\theta$  angle range of 10° to 80° using the LYNXEYE detector (Lyncean Technologies, Fremont, CA, USA). Their surface functional groups were identified using a VERTEX 70v FTIR spectrometer (Billerica, MA, USA), and the spectra

were collected within the range of 4000–400  $\text{cm}^{-1}$ , with a spectral resolution of 4  $\text{cm}^{-1}$  and an average of 64 scans. Thermogravimetric and differential thermal analysis (TGA-DTA) was used to analyze the thermal stability of the pseudo-boehmite at temperatures ranging from 25 to 800  $^{\circ}\text{C}$ , using a Labsys evo thermal analyzer (Setaram, Lyon, France) with a heating rate of 5  $^{\circ}\text{C}/\text{min}$ . Scanning electron microscopy (SEM) combined with energy-dispersive spectroscopy (EDS) (JEOL JSM-IT500HR (JEOL Ltd., Akishima, Tokyo, Japan)) was used to determine the surface morphology and microstructure of the  $\gamma\text{-AlOOH}$  and  $\gamma\text{-Al}_2\text{O}_3$  particles before and after adsorption. The nitrogen adsorption–desorption isotherms of both materials were collected using a Micromeritics Instrument (Micromeritics Gemini VII 1014 (Micromeritics Instrument Corporation, Norcross, GA, USA) operating at a liquid nitrogen temperature of 77 K, covering a relative pressure range of 0.001 to 0.998 to obtain the Brunauer–Emmett–Teller (BET) specific surface area. To calculate the EBT removal efficiency, absorbance was measured for each test after filtration using a UV-vis spectrophotometer (DR 6000 UV-vis (Hach, Berlin, Germany)).

The pH drift approach, based on the salt addition method, was used to calculate the point of zero charge (pzc). The pzc values for  $\gamma\text{-AlOOH}$  and  $\gamma\text{-Al}_2\text{O}_3$  were determined in a solution of NaCl (0.01 M) at 25  $^{\circ}\text{C}$ . In this method, 100 mg of each sample and 50 mL of NaCl (0.01 M) were mixed in a series of beakers. After that, 0.1 M NaOH and 0.1 M HCl solutions were used to bring the suspensions' pH values back to the range of 2–12. The beakers were vigorously stirred in a shaking bath for 48 h at a stirring speed of 250 rpm [28]. After settling, the final pH of each suspension was measured. The initial pH at which  $\Delta\text{pH}$  is equal to zero was taken as the pzc.

### 3.4. Adsorption Study

#### 3.4.1. Dye's Stock Solutions

A stock solution of Eriochrome black T (EBT) was prepared with a concentration of 1  $\text{g L}^{-1}$ . Subsequently, a series of dilutions were carried out to achieve the desired concentrations using distilled water.

#### 3.4.2. Initial Studies

The initial investigation focused on assessing the EBT dye removal in relation to pH variations. The pH of the solutions was adjusted to the desired values using either 0.1 M NaOH or 0.1 M HCl. To carry out the experiment, beakers containing a fixed mass of adsorbent (50 mg) were filled with 50 mL of the dye solution (50  $\text{mg L}^{-1}$ ). The beakers, adjusted to the required pH, were subjected to continuous stirring for 180 min at 25  $^{\circ}\text{C}$  using a multi-station shaker. The influence of the adsorbent mass (ranging from 5 to 300 mg) on the dye adsorption process was also investigated.

The collected data were used to calculate the removal efficiency (%) and the amount of dye adsorbed ( $\text{mg g}^{-1}$ ) using Equations (1) and (2), respectively.

$$q_e = \frac{(C_0 - C_e)}{m} * V \quad (1)$$

$$\% \text{ Removal efficiency} = \frac{(C_0 - C_e)}{C_0} * 100 \quad (2)$$

$q_e$ : Equilibrium adsorption capacity ( $\text{mg g}^{-1}$ )

$C_0$ : Dye's initial concentration ( $\text{mg L}^{-1}$ )

$C_e$ : Dye's equilibrium concentration ( $\text{mg L}^{-1}$ )

$V$ : Dye's solution volume (L)

$m$ : Adsorbent mass (g)

#### 3.4.3. Kinetic Adsorption Models

The examination of adsorption kinetics allows the determination of the time required for the adsorption process to reach equilibrium. Various kinetic models, including pseudo-

first-order (Equation (3)), pseudo-second-order (Equation (4)) and intraparticle diffusion (Equation (5)) models, are used to ascertain the adsorption process' kinetics [38–40].

$$q_t = q_e(1 - \exp(-k_1t)) \quad (3)$$

$$q_t = \frac{k_2q_e^2t}{1 + k_2q_e t} \quad (4)$$

$$q_t = k_i t^{0.5} + C \quad (5)$$

where

$q_t$ : Adsorbed dye at time  $t$  ( $\text{mg g}^{-1}$ )

$q_e$ : Equilibrium adsorbed dye ( $\text{mg g}^{-1}$ )

$k_1$  ( $\text{min}^{-1}$ ),  $k_2$  ( $\text{g mg}^{-1} \text{min}^{-1}$ ),  $k_i$  ( $\text{g mg}^{-1} \text{min}^{-0.5}$ ): Equilibrium rate constant characteristics of the pseudo-first-order, pseudo-second-order and intraparticle diffusion models, respectively.

$C$ : Constant associated with the boundary layer's thickness ( $\text{mg g}^{-1}$ )

The EBT adsorption kinetics were investigated by adding 50 mg of adsorbent to 50 mL of the dye solution ( $50 \text{ mg L}^{-1}$ ). The mixture was continuously stirred and monitored at room temperature ( $25 \text{ }^\circ\text{C}$ ) for a contact time ranging from 2 to 240 min. Samples were then taken at different times. The kinetic models described above were used to fit the experimental data. The adsorption kinetics constants for each model and the correlation coefficients ( $R^2$ ) values were determined.

#### 3.4.4. Isotherm Adsorption Models

The batch equilibration method was employed to determine the adsorption isotherms at  $25 \text{ }^\circ\text{C}$  [41]. Then, 50 mg of adsorbent was added to 50 mL of dye solution, at concentrations ranging from 50 to  $500 \text{ mg L}^{-1}$ ; the system was allowed to reach equilibrium by maintaining a contact time of 24 h. The resulting experimental data were fitted to Langmuir (Equation (6)) and Freundlich (Equation (7)) isotherm models.

$$q_e = \frac{K_L q_m C_e}{1 + K_L C_e} \quad (6)$$

$$q_e = K_f C_e^{1/n} \quad (7)$$

where  $C_e$  is the solution's equilibrium concentration ( $\text{mg L}^{-1}$ ),  $K_L$  is the Langmuir equilibrium constant ( $\text{L mg}^{-1}$ ),  $q_m$  represents the maximum adsorption capacity of the adsorbent to form a monolayer ( $\text{mg g}^{-1}$ ), while  $q_e$  ( $\text{mg g}^{-1}$ ) denotes the amount of dye adsorbed at equilibrium. The Freundlich constants,  $K_f$  ( $\text{mg g}^{-1}$ ) and  $n$ , are associated with the adsorption capacity and intensity of the adsorbent, respectively. Slope  $1/n$  is a measure of the surface heterogeneity; as it approaches zero, the surface becomes more heterogeneous.

#### 3.4.5. Thermodynamic Studies

In order to gain a better insight into the influence of temperature on the adsorption process, thermodynamic studies were carried out at different temperatures ( $20, 30, 40 \text{ }^\circ\text{C}$ ), keeping the other parameters constant (solution's pH, adsorbent mass 50 mg, dye concentration  $50 \text{ mg L}^{-1}$ , contact time 3 h). The mixture was continuously stirred in a double-walled beaker at the set temperature. Equation (8) through (10) were used to estimate the thermodynamic variables, including changes in the Gibbs free energy ( $\Delta G^\circ$ ) ( $\text{J mol}^{-1}$ ), free enthalpy ( $\Delta H^\circ$ ) ( $\text{J mol}^{-1}$ ), and entropy ( $\Delta S^\circ$ ) ( $\text{J mol}^{-1} \text{K}^{-1}$ ):

$$\Delta G^\circ = -RT \ln(K_d) \quad (8)$$

$$\Delta G^\circ = \Delta H^\circ - T\Delta S^\circ \quad (9)$$

$$\ln(K_d) = \frac{\Delta S^\circ}{R} - \frac{\Delta H^\circ}{RT} \quad (10)$$

where ( $R = 8.314 \text{ J mol}^{-1} \text{ K}^{-1}$ ) is the universal gas constant,  $T(\text{K})$  is the temperature used and  $K_d$  is the thermodynamic equilibrium constant. The change in free enthalpy ( $\Delta H^\circ$ ) and entropy ( $\Delta S^\circ$ ) can be obtained from the slope and intercept of the plot of  $\ln(K_d)$  versus  $(1/T)$  using the van 't Hoff formula presented in (Equation (10)) [29,42].

#### 4. Conclusions

The adsorption capacity of  $\gamma$ -AlOOH particles, synthesized through the precipitation method, was evaluated for EBT dye removal. The  $\text{N}_2$  adsorption–desorption isotherms indicate that the  $\gamma$ -AlOOH particles have a BET surface area of  $298.35 \text{ m}^2 \text{ g}^{-1}$ . The thermal conversion of  $\gamma$ -AlOOH at  $800 \text{ }^\circ\text{C}$  for 3.0 h leads to the formation of  $\gamma$ - $\text{Al}_2\text{O}_3$ , whose BET surface area is  $403.31 \text{ m}^2 \text{ g}^{-1}$ . Both adsorbents show promising adsorption capacities for EBT.

Investigation of the isotherms revealed a close correlation with the Langmuir isotherm model, with maximum adsorption capacities of  $344.44 \text{ mg g}^{-1}$  and  $421.94 \text{ mg g}^{-1}$  for  $\gamma$ -AlOOH and  $\gamma$ - $\text{Al}_2\text{O}_3$ , respectively. The kinetic data are in good agreement with the pseudo-second-order kinetic model. The EBT removal efficiency increases with rising temperature. The enthalpy of adsorption shows that physisorption is involved. The XRD patterns before and after adsorption, along with the SEM images and EDS spectrum, are in good agreement with the adsorption results.

The synthesis of  $\gamma$ -AlOOH and the production of  $\gamma$ - $\text{Al}_2\text{O}_3$  through thermal conversion could offer promising prospects for the valorization of drinking water treatment sludge as a potential adsorbent for the removal of environmentally harmful dyes. This approach effectively addresses two major concerns: on the one hand, public concern regarding the environmental issues associated with drinking water treatment sludge, and on the other hand, the recycling and reuse of novel and efficient materials for water treatment purposes.

**Author Contributions:** I.B.: Conceptualization, Methodology, Investigation, Writing the original version, S.K.: Conceptualization, revision, supervision, J.N.: Conceptualization, revision, supervision, Z.B.: Revision. All authors have read and agreed to the published version of the manuscript.

**Funding:** This research did not benefit from any specific grants from funding agencies in the public, commercial or non-profit sectors.

**Data Availability Statement:** The original contributions presented in the study are included in the article, further inquiries can be directed to the corresponding authors.

**Conflicts of Interest:** The authors declare no conflicts of interest.

#### References

1. Wang, D.; Li, Z.; Lv, F.; Guan, M.; Chen, J.; Wu, C.; Li, Y.; Li, Y.; Zhang, W. Characterization of microspheres  $\gamma$ -AlOOH and the excellent removal efficiency of Congo red. *J. Phys. Chem. Solids* **2022**, *174*, 111043. [CrossRef]
2. Ardila-Leal, L.D.; Poutou-Piñales, R.A.; Pedroza-Rodríguez, A.M.; Quevedo-Hidalgo, B.E. A brief history of colour, the environmental impact of synthetic dyes and removal by using laccases. *Molecules* **2021**, *26*, 3813. [CrossRef] [PubMed]
3. Ihaddaden, S.; Aberkane, D.; Boukerroui, A.; Robert, D. Removal of methylene blue (basic dye) by coagulation-flocculation with biomaterials (bentonite and *Opuntia ficus indica*). *J. Water Process. Eng.* **2022**, *49*, 102952. [CrossRef]
4. Liu, T.; Wang, Z.; Wang, X.; Yang, G.; Liu, Y. Adsorption-photocatalysis performance of polyaniline/dicarboxyl acid cellulose@graphene oxide for dye removal. *Int. J. Biol. Macromol.* **2021**, *182*, 492–501. [CrossRef] [PubMed]
5. Li, X.; Xu, J.; Luo, X.; Shi, J. Efficient adsorption of dyes from aqueous solution using a novel functionalized magnetic biochar: Synthesis, kinetics, isotherms, adsorption mechanism, and reusability. *Bioresour. Technol.* **2022**, *360*, 127526. [CrossRef] [PubMed]
6. Crini, G.; Lichtfouse, E.; Wilson, L.D.; Morin-Crini, N. Conventional and non-conventional adsorbents for wastewater treatment. *Environ. Chem. Lett.* **2019**, *17*, 195–213. [CrossRef]
7. Fernandes, E.P.; Silva, T.S.; Carvalho, C.M.; Selvasembian, R.; Chaukura, N.; Oliveira, L.M.; Meneghetti, S.M.P.; Meili, L. Efficient adsorption of dyes by  $\gamma$ -alumina synthesized from aluminum wastes: Kinetics, isotherms, thermodynamics and toxicity assessment. *J. Environ. Chem. Eng.* **2021**, *9*, 106198. [CrossRef]
8. Mahinroosta, M.; Allahverdi, A. Pilot-scale valorization of hazardous aluminum dross into  $\gamma$ - $\text{Al}_2\text{O}_3$  nanoadsorbent for efficient removal of fluoride. *Environ. Technol. Innov.* **2021**, *23*, 101549. [CrossRef]
9. Keshtkar, Z.; Tamjidi, S.; Vaferi, B. Intensifying nickel (II) uptake from wastewater using the synthesized  $\gamma$ -alumina: An experimental investigation of the effect of nano-adsorbent properties and operating conditions. *Environ. Technol. Innov.* **2021**, *22*, 101439. [CrossRef]



10. Van Truong, T.; Kim, D.-J. Synthesis of high quality boehmite and  $\gamma$ -alumina for phosphorus removal from water works sludge by extraction and hydrothermal treatment. *Environ. Res.* **2022**, *212*, 113448. [[CrossRef](#)]
11. Ali, S.; Abbas, Y.; Zuhra, Z.; Butler, I.S. Synthesis of  $\gamma$ -alumina ( $\text{Al}_2\text{O}_3$ ) nanoparticles and their potential for use as an adsorbent in the removal of methylene blue dye from industrial wastewater. *Nanoscale Adv.* **2019**, *1*, 213–218. [[CrossRef](#)]
12. Yang, W.; Li, C.; Tian, S.; Liu, L.; Liao, Q. Influence of synthesis variables of a sol-gel process on the properties of mesoporous alumina and their fluoride adsorption. *Mater. Chem. Phys.* **2020**, *242*, 122499. [[CrossRef](#)]
13. Zhou, J.; Cai, W.; Yang, Z.; Xia, Q.; Chen, J.; Fan, J.; Du, C. N,N-dimethylformamide assisted facile hydrothermal synthesis of boehmite microspheres for highly effective removal of Congo red from water. *J. Colloid. Interface Sci.* **2021**, *583*, 128–138. [[CrossRef](#)] [[PubMed](#)]
14. Ballou, I.; Kounbach, S.; Naja, J.; Bakher, Z.E.; Laraki, K.; Raibi, F.; Saadi, R.; Kholtei, S. A new approach of aluminum extraction from drinking water treatment sludge using ammonium sulfate roasting process. *Miner. Eng.* **2022**, *189*, 107859. [[CrossRef](#)]
15. Gomez, M.; Pizarro, J.; Castillo, X.; Diaz, C.; Ghisolfi, A.; Chavez, M.d.L.; Cazorla-Amoros, D.; Arenas-Alatorre, J. Preparation of mesoporous  $\gamma$ - $\text{Al}_2\text{O}_3$  with high surface area from an ALOOH extract of recycling biomass ash. *J. Environ. Chem. Eng.* **2021**, *9*, 105925. [[CrossRef](#)]
16. Gai, W.-Z.; Zhang, S.-H.; Yang, Y.; Zhang, X.; Deng, Z.-Y. Separation of Excess Fluoride from Water Using Amorphous and Crystalline ALOOH Adsorbents. *ACS Omega* **2021**, *6*, 16488–16497. [[CrossRef](#)] [[PubMed](#)]
17. Du, X.; Wang, Y.; Su, X.; Li, J. Influences of pH value on the microstructure and phase transformation of aluminum hydroxide. *Powder Technol.* **2009**, *192*, 40–46. [[CrossRef](#)]
18. Khazaei, A.; Nazari, S.; Karim, G.; Ghaderi, E.; Moradian, K.M.; Bagherpor, Z.; Nazari, S. Synthesis and Characterization of  $\gamma$ -Alumina Porous Nanoparticles from Sodium Aluminate Liquor with Two Different Surfactants. *Int. J. Nanosci. Nanotechnol.* **2016**, *12*, 207–214.
19. Milanović, M.; Obrenović, Z.; Stijepović, I.; Nikolić, L.M. Nanocrystalline boehmite obtained at room temperature. *Ceram. Int.* **2018**, *44*, 12917–12920. [[CrossRef](#)]
20. Kam, O.R.; Bakouan, C.; Zongo, I.; Guel, B. Removal of Thallium from Aqueous Solutions by Adsorption onto Alumina Nanoparticles. *Processes* **2022**, *10*, 1826. [[CrossRef](#)]
21. Yaya, I.M.; Guillaume, N.; Arkhis, M. The Synthesis of Mesoporous Pseudoboehmite by A Route Mineral and its Transformation into Alumina- $\gamma$ . *Mat. Sci. Ind. J.* **2018**, *16*, 140.
22. Miranda, R.; Latour, I.; Blanco, A. Silica removal from a paper mill effluent by adsorption on pseudoboehmite and  $\gamma$ - $\text{Al}_2\text{O}_3$ . *Water* **2021**, *13*, 2031. [[CrossRef](#)]
23. Sun, T.; Zhuo, Q.; Chen, Y.; Wu, Z. Synthesis of boehmite and its effect on flame retardancy of epoxy resin. *High. Perform. Polym.* **2015**, *27*, 100–104. [[CrossRef](#)]
24. Khan, H.; Iram, Gul, K.; Ara, B.; Khan, A.; Ali, N.; Ali, N.; Bilal, M. Adsorptive removal of acrylic acid from the aqueous environment using raw and chemically modified alumina: Batch adsorption, kinetic, equilibrium and thermodynamic studies. *J. Environ. Chem. Eng.* **2020**, *8*, 103927. [[CrossRef](#)]
25. Tolède, R.R.; Santoyo, V.R.; Sánchez, D.M.; Rosales, M.M. Efecto del precursor de aluminio en las propiedades fisicoquímicas de la  $\gamma$ - $\text{Al}_2\text{O}_3$  por el método hidrólisis/precipitación. *SciELO Anal.* **2022**, *10*, 20.
26. Wang, L.Y.; Tong, D.S.; Zhao, L.Z.; Liu, F.G.; An, N.; Yu, W.H.; Zhou, C.H. Utilization of alum sludge for producing aluminum hydroxide and layered double hydroxide. *Ceram. Int.* **2014**, *40*, 15503–15514. [[CrossRef](#)]
27. Sun, Y.; Ding, C.; Cheng, W.; Wang, X. Simultaneous adsorption and reduction of U(VI) on reduced graphene oxide-supported nanoscale zerovalent iron. *J. Hazard. Mater.* **2014**, *280*, 399–408. [[CrossRef](#)] [[PubMed](#)]
28. Li, J.; Wang, H.; Zhu, R.; Chang, H.; Xiong, G.; Wu, J.; Feng, H.; Li, P. Economical Synthesis of High Surface Area  $\gamma$ - $\text{Al}_2\text{O}_3$  for the Adsorption of Organic Pollutant from Wastewater. *Am. J. Chem. Eng.* **2020**, *8*, 76. [[CrossRef](#)]
29. El Gaayda, J.; Akbour, R.A.; Titchou, F.E.; Afanga, H.; Zazou, H.; Swanson, C.; Hamdani, M. Uptake of an anionic dye from aqueous solution by aluminum oxide particles: Equilibrium, kinetic, and thermodynamic studies. *Groundw. Sustain. Dev.* **2020**, *12*, 100540. [[CrossRef](#)]
30. Kecira, Z.; Benturki, O.; Benturki, A.; Daoud, M.; Girods, P. High adsorption capacity of nitrobenzene from aqueous solution using activated carbons prepared from vegetable waste. *Environ. Prog. Sustain. Energy* **2020**, *39*, 13463. [[CrossRef](#)]
31. Labaali, Z.; Kholtei, S.; Naja, J.  $\text{Co}^{2+}$  removal from wastewater using apatite prepared through phosphate waste rocks valorization: Equilibrium, kinetics and thermodynamics studies. *Sci. Afr.* **2020**, *8*, e00350. [[CrossRef](#)]
32. Khan, A.; Wang, X.; Gul, K.; Khuda, F.; Aly, Z.; Elseman, A. Microwave-assisted spent black tea leaves as cost-effective and powerful green adsorbent for the efficient removal of Eriochrome black T from aqueous solutions. *Egypt. J. Basic. Appl. Sci.* **2018**, *5*, 171–182. [[CrossRef](#)]
33. Manzar, M.S.; Khan, G.; Lins, P.V.d.S.; Zubair, M.; Khan, S.U.; Selvasembian, R.; Meili, L.; Blaisi, N.I.; Nawaz, M.; Aziz, H.A.; et al. RSM-CCD optimization approach for the adsorptive removal of Eriochrome Black T from aqueous system using steel slag-based adsorbent: Characterization, Isotherm, Kinetic modeling and thermodynamic analysis. *J. Mol. Liq.* **2021**, *339*, 116714. [[CrossRef](#)]
34. Zubair, M.; Aziz, H.A.; Ihsanullah, I.; Ahmad, M.A.; Al-Harathi, M.A. Biochar supported CuFe layered double hydroxide composite as a sustainable adsorbent for efficient removal of anionic azo dye from water. *Environ. Technol. Innov.* **2021**, *23*, 101614. [[CrossRef](#)]

35. Chatla, A.; Almanassra, I.W.; Kochkodan, V.; Laoui, T.; Alawadhi, H.; Atieh, M.A. Efficient Removal of Eriochrome Black T (EBT) Dye and Chromium (Cr) by Hydrotalcite-Derived Mg-Ca-Al Mixed Metal Oxide Composite. *Catalysts* **2022**, *12*, 1247. [[CrossRef](#)]
36. Hajjaoui, H.; Khnifira, M.; Soufi, A.; Abdennouri, M.; Akkaya, S.; Akkaya, R.; Barka, N. Experimental, DFT and MD simulation studies of Mordant Black 11 dye adsorption onto polyaniline in aqueous solution. *J. Mol. Liq.* **2022**, *364*, 120045. [[CrossRef](#)]
37. Sepehri, S.; Rezaei, M.; Garbarino, G.; Busca, G. Facile synthesis of a mesoporous alumina and its application as a support of Ni-based autothermal reforming catalysts. *Int. J. Hydrogen Energy* **2016**, *41*, 3456–3464. [[CrossRef](#)]
38. Revellame, E.D.; Fortela, D.L.; Sharp, W.; Hernandez, R.; Zappi, M.E. adsorption kinetic modeling using pseudo-first order and pseudo-second order rate laws: A review. *Clean. Eng. Technol.* **2020**, *1*, 100032. [[CrossRef](#)]
39. Salama, A.; Abou-Zeid, R.E. Ionic chitosan/silica nanocomposite as efficient adsorbent for organic dyes. *Int. J. Biol. Macromol.* **2021**, *188*, 404–410. [[CrossRef](#)]
40. Ghibate, R.; Senhaji, O.; Taouil, R. Kinetic and thermodynamic approaches on Rhodamine B adsorption onto pomegranate peel. *Case Stud. Chem. Environ. Eng.* **2020**, *3*, 100078. [[CrossRef](#)]
41. El Hassani, K.; Beakou, B.H.; Kalnina, D.; Oukani, E.; Anouar, A. Effect of morphological properties of layered double hydroxides on adsorption of azo dye Methyl Orange: A comparative study. *Appl. Clay Sci.* **2017**, *140*, 124–131. [[CrossRef](#)]
42. Hegde, V.; Uthappa, U.T.; Mane, P.; Ji, S.M.; Suneetha, M.; Wang, B.; Altalhi, T.; Subrahmanya, T.M.; Kurkuri, M.D. Design of low-cost natural casein biopolymer-based adsorbent for efficient adsorption of multiple anionic dyes and diclofenac sodium from aqueous solutions. *Chemosphere* **2024**, *353*, 141571. [[CrossRef](#)]

**Disclaimer/Publisher's Note:** The statements, opinions and data contained in all publications are solely those of the individual author(s) and contributor(s) and not of MDPI and/or the editor(s). MDPI and/or the editor(s) disclaim responsibility for any injury to people or property resulting from any ideas, methods, instructions or products referred to in the content.